A new petrogenetic model for low-Ca boninites: Evidence from veined sub-arc xenoliths on melt-mantle interaction and melt fractionation

A. Bénard, D. A. Ionov

Geochemistry Geophysics Geosystems G3

Article
Volume 13, Number 1
28 June 2012
Q0AF05, doi:10.1029/2012GC004145
ISSN: 1525-2027

Published by AGU and the Geochemical Society

A new petrogenetic model for low-Ca boninites: Evidence from veined sub-arc xenoliths on melt-mantle interaction and melt fractionation

A. Bénard and D. A. Ionov

Université Jean Monnet, PRES Université de Lyon, UMR6524-CNRS, FR-42023 Saint-Étienne, France (antoine.benard@univ-st-etienne.fr)

[1] Low-Ca boninites (LCB) are arc-related magmatic rocks enriched in large ion lithophile elements (LILE), light rare earth elements (LREE), Zr and Hf relative to medium to heavy REE (MREE-HREE). These signatures are commonly attributed to a unique slab-derived agent that metasomatized a depleted mantle source but their origin in such an agent remains enigmatic. We report andesite-hosted refractory spinel harzburgite xenoliths from the Kamchatka arc, which contain a series of orthopyroxene-rich veins; these veins range in thickness, the contents of clinopyroxene and amphibole and degrees of reaction with the host. Vein minerals in reaction zones with host harzburgites show progressive depletion in MREE-HREE at constant Zr-Hf and develop patterns (U-shaped REE with Zr-Hf spikes) that mimic those of LCB. Major and trace element modeling suggests that these veins (1) formed from a high-temperature (≥1400°C), MgO-rich (∼30 wt.%) and silicic (∼54 wt.% SiO_2) initial melt, strongly depleted in Al_2O_3, TiO_2 and alkalis and (2) record fractionation of the initial melt to form hydrous liquids; the initial melt was equilibrated with metasomatized Kamchatka harzburgites and was similar in trace element abundances to island arc tholeiite (LREE-depleted to flat LREE-MREE patterns, low Nb and Ta but no significant Zr-Hf anomalies, high LILE). We argue that primary magmas of LCB formed by fluid-fluxed (LILE-rich and [Nb, Ta]-depleted fluid) melting of a cpx-free, highly refractory (≥30% melt extraction) harzburgitic source similar to arc peridotites from Kamchatka and elsewhere. This peculiar source may explain the distinctive major element features of LCB primary magmas. We propose that the primary magmas of LCB develop their characteristic trace element patterns through fractionation and reaction with refractory peridotites in the mantle wedge. Slab-related components alone may explain the high LILE in LCB but not their distinctive REE patterns and positive Zr-Hf anomalies.

Components: 8800 words, 4 figures, 3 tables.

Keywords: island arc; low-Ca boninite; mantle xenolith; melt-rock interaction; modeling.

Index Terms: 1031 Geochemistry: Subduction zone processes (3060, 3613, 8170, 8413); 1037 Geochemistry: Magma genesis and partial melting (3619); 1065 Geochemistry: Major and trace element geochemistry.

Received 14 March 2012; **Revised** 3 May 2012; **Accepted** 14 May 2012; **Published** 28 June 2012.

Bénard, A., and D. A. Ionov (2012), A new petrogenetic model for low-Ca boninites: Evidence from veined sub-arc xenoliths on melt-mantle interaction and melt fractionation, *Geochem. Geophys. Geosyst.*, *13*, Q0AF05, doi:10.1029/2012GC004145.

Theme: Assessing Magmatic, Neovolcanic, Hydrothermal, and Biological Processes along Intra-Oceanic Arcs and Back-Arcs

1. Introduction

[2] Boninites are enigmatic arc-related volcanic rocks that have higher SiO_2 (>52 wt.%), MgO (>8 wt.%) and H_2O (≥1.5 wt.%) and lower TiO_2 than those from island arc tholeiite suites [*Falloon and Danyushevsky*, 2000; *Le Bas*, 2000]. High- and low-Ca boninites (LCB) are distinguished on the basis of a bulk rock Al_2O_3/CaO ratio threshold at 0.75 [*Crawford et al.*, 1989]. LCB were reported from several Western Pacific island arcs [*Cameron*, 1989; *Hickey and Frey*, 1982]. They contain orthopyroxene (opx) and less common clinopyroxene (cpx) surrounding corroded Mg-rich ($Fo_{92–94}$) olivine [*Walker and Cameron*, 1983]. Bulk rock LCB have U-shaped or light rare earth element (LREE)-enriched REE patterns and high Zr and Hf relative to medium REE (MREE) [*Taylor et al.*, 1994].

[3] The origin of LCB is usually attributed to re-melting of depleted mantle lithosphere fluxed by slab-derived hydrous agents [*Cameron et al.*, 1979; *Crawford et al.*, 1989; *Hickey and Frey*, 1982]. Some models imply that trace element budgets of LCB are dominated by melts and/or fluids, which selectively mobilize large ion lithophile elements (LILE), LREE, Zr and Hf from the slab and transport these incompatible elements to the melting region [*König et al.*, 2010; *Taylor et al.*, 1994], i.e., the characteristic trace element patterns of LCB are assumed to mimic those of slab-derived components added to a depleted source [*Hickey and Frey*, 1982; *Taylor et al.*, 1994]. Other models attribute the unusual Zr-Hf spikes of LCB to mantle source effects such as partial melting controlled by Zr-Hf-rich opx in depleted harzburgite [*Kamenetsky et al.*, 2002] or melting of mafic veins in harzburgites [*Pearce et al.*, 1999]. In any case, these models fail to explain the lack of correlation between ubiquitous Zr-Hf enrichments and either radiogenic isotope compositions, e.g., ε_{Nd} and ε_{Hf} [*König et al.*, 2010; *Pearce et al.*, 1999], or MREE to heavy REE (HREE) ratios [e.g., *Kamenetsky et al.*, 2002; *Reagan et al.*, 2010] from one LCB location to another.

[4] Recent studies of websteritic veins in peridotite xenoliths from the andesitic volcano Avacha in Kamchatka (Russia) outlined the presence of remnants of percolating boninitic melts [*Halama et al.*, 2009]. We present major and trace element data and modeling on new types of opx-rich veins of mantle origin cutting peridotite xenoliths from Avacha. These veins may have formed from LCB melts infiltrating sub-arc lithospheric mantle. We demonstrate that the characteristic trace element patterns of LCB can be acquired by an initial melt with a typical subduction-related signature similar to that of island arc tholeiite (LREE-depleted to flat REE patterns, low Nb and Ta but no significant Zr-Hf anomalies and high LILE contents) through a combination of (1) melt fractionation in the mantle controlling trace element enrichment and (2) re-equilibration and reaction with host peridotite to produce MREE-HREE depletion at constant Zr-Hf abundances.

2. Analytical Techniques

[5] Major element abundances in minerals were measured in thick (120 μm) polished sections by Electron Probe Micro-Analysis (EPMA), using a CAMECA SX-100 instrument at the Laboratoire Magmas et Volcans (Clermont-Ferrand) with an accelerating voltage of 15 kV and a current of 15 nA. Counting times were 5–10 s on background and 20 s (Ni), 15 s (Ca and Ti) and 10 s for all other elements on peaks. Matrix effects were corrected using Phi (r) z modeling with Peak Sight© software from CAMECA™.

[6] Trace element analyses were done by Inductively Coupled Plasma Mass-Spectrometry (ICPMS) at the Laboratoire Géosciences Montpellier, Université Montpellier II with a FINNIGAN™ Element-2 system. Minerals were analyzed in thick sections by Laser-Ablation (LA) ICPMS using a MICROLAS (Geolas Q+) platform with a EXCIMER CompEx 102 laser at 8 Hz, beam energy of 12 J.cm^{-2} and spot size of 51–77 μm (amphibole [amph] and cpx) and 122 μm (opx). The NIST 612 and NIST 610 glass standards were used for calibration. Ca and Si were used as internal standards; BCR-2g sample was measured for quality control (Table 1). Bulk vein powders (~50 mg) were dissolved in HF-$HClO_4$ mixtures; dried samples were taken up in HNO_3 and diluted to 1:2000 in 2% HNO_3 shortly before the analysis [*Ionov et al.*, 1992]. Chemical blanks and BIR-1 basaltic reference material were run with the samples (Table 2).

3. Geological Setting and Samples

[7] Avacha is an active strato-volcano in the Eastern Volcanic Front related to fast subduction (7–9 cm/a) of the ~80 My old Pacific plate beneath south Kamchatka (Figure 1a). Avacha is located ~120 km above the slab; low P wave velocity domains beneath the Moho are consistent with the presence of melt [*Gorbatov et al.*, 1997]. Xenoliths in this

Table 1. Representative Major (wt.%) and Trace Element (ppm) Data for Vein Minerals and BCR-2g Reference Material[a]

	Type A Vein			Type B1 Vein			Type B1 Vein-r.z.			Type B2 Vein			h.r.	n.a.
	opx core	opx rim	amph	opx	cpx	amph	cpx	cpx	cpx	opx	cpx	amph	cpx	BCR-2g
SiO_2	58.25	56.65	50.72	57.14	53.43	48.16	53.94	53.45	54.44	56.84	53.26	46.25	54.52	-
TiO_2	-	0.02	0.21	0.04	0.06	0.11	0.01	0.06	0.06	-	0.06	0.06	-	-
Al_2O_3	0.51	1.76	7.59	1.32	2.07	10.81	1.46	2.12	1.45	2.93	2.51	11.16	0.96	-
Cr_2O_3	0.01	0.67	0.57	0.41	0.87	0.44	0.75	0.60	0.76	0.17	0.85	2.30	0.32	-
FeO	5.96	6.13	3.03	6.70	2.78	4.39	2.73	2.74	2.78	6.09	3.05	3.70	2.19	-
MnO	0.08	0.15	0.02	0.18	0.07	0.11	0.11	0.11	0.11	0.13	0.04	0.09	0.06	-
MgO	35.21	33.46	20.89	33.26	17.52	19.54	17.76	17.40	17.68	33.66	17.30	18.89	18.20	-
CaO	0.29	0.94	12.49	0.96	22.79	11.36	22.83	23.02	22.70	0.37	22.73	11.86	24.15	-
Na_2O	0.05	0.03	1.34	0.02	0.27	2.13	0.19	0.21	0.32	0.01	0.23	2.36	0.09	-
K_2O	0.01	0.00	0.82	-	-	-	-	-	-	-	-	0.31	-	-
Total	100.50	99.89	97.79	100.09	99.95	96.34	99.83	99.79	100.36	100.25	100.07	97.10	100.54	-
Mg#[b]	0.913	0.907	0.925	0.898	0.918	0.880	0.921	0.919	0.919	0.908	0.910	0.901	0.937	-
Li	0.644	0.62	0.738	0.608	1.93	1.01	2.08	1.38	0.930	0.718	0.760	1.23	0.872	9.84
Sc	3.20	4.73	27	22	85	63	86	69	78	18	88	88	82	33
V	105	53	221	77	263	386	274	213	181	61	180	346	190	430
Co	-	-	38	60	-	44	113	52	24	56	22	68	-	-
Ni	-	-	481	652	-	1760	2728	1244	867	622	331	1603	-	-
Zn	80	74	22	39	59	23	63	28	8.76	35	9.39	26	13	-
Rb	-	0.034	0.836	0.0089	0.159	0.802	0.219	-	0.058	-	-	0.681	-	52
Sr	0.007	0.253	14	0.695	27	116	25	11	6.44	0.026	18	48	11	334
Y	0.044	0.142	1.97	0.272	1.94	4.92	1.62	1.22	0.577	0.026	0.410	0.733	0.671	31
Zr	0.149	0.038	0.681	0.349	3.88	16	6.92	7.64	4.91	0.499	7.83	11	0.419	168
Nb	-	0.007	0.132	-	0.016	0.459	0.050	0.025	0.022	0.004	0.005	0.199	0.004	11
Ba	0.010	0.781	30	0.362	3.93	35	6.40	0.597	0.751	0.040	0.011	36	1.22	655
La	0.003	0.011	0.387	0.010	0.234	0.895	0.321	0.212	0.193	0.001	0.445	0.853	0.096	25
Ce	0.005	0.049	1.40	0.029	0.82	3.20	1.05	0.733	0.553	0.004	1.23	2.33	0.238	51
Pr	-	0.007	0.220	0.006	0.138	0.553	0.153	0.122	0.081	0.001	0.156	0.295	0.037	6.57
Nd	0.004	0.048	0.876	0.041	0.751	2.81	0.718	0.512	0.288	0.005	0.537	0.982	0.163	27
Sm	0.003	0.017	0.229	0.015	0.280	0.792	0.159	0.135	0.057	0.006	0.047	0.119	0.063	6.26
Eu	0.001	0.006	0.156	0.006	0.097	0.296	0.062	0.065	0.031	-	0.020	0.036	0.019	1.93
Gd	-	0.023	0.211	0.020	0.272	0.805	0.195	0.140	0.036	-	0.024	0.074	0.033	7.12
Tb	0.000	0.004	0.043	0.002	0.043	0.131	0.027	0.027	0.0067	0.001	0.004	0.011	0.011	1.06
Dy	0.004	0.040	0.337	0.031	0.332	0.898	0.244	0.190	0.064	0.001	0.038	0.083	0.081	5.69
Ho	0.001	0.008	0.070	0.011	0.075	0.196	0.061	0.055	0.021	-	0.014	0.024	0.020	1.19
Er	0.008	0.028	0.240	0.021	0.222	0.580	0.227	0.146	0.081	0.004	0.070	0.125	0.105	3.59
Tm	0.002	0.007	0.045	0.009	0.040	0.092	0.039	0.024	0.017	0.002	0.017	0.029	0.023	0.621
Yb	0.013	0.042	0.299	0.070	0.279	0.667	0.286	0.239	0.164	0.024	0.182	0.267	0.178	2.90
Lu	0.003	0.008	0.046	0.014	0.054	0.102	0.052	0.053	0.031	0.006	0.030	0.046	0.037	0.467
Hf	0.001	0.003	0.038	0.017	0.137	0.611	0.220	0.248	0.109	0.016	0.272	0.354	0.005	4.53
Ta	-	-	0.007	0.001	-	0.027	-	0.003	0.002	-	0.001	0.017	-	0.714
Pb	0.013	0.025	0.082	0.021	0.128	0.195	0.089	0.123	0.098	0.006	0.115	0.166	0.109	11
Th	0.014	0.031	0.030	0.003	0.016	0.015	0.028	0.025	0.0094	0.004	0.011	0.028	0.009	5.48
U	0.005	0.017	0.0183	-	0.006	0.0135	0.039	0.057	0.0113	-	0.004	0.004	0.008	1.64

[a]BCR-2g reference material was analyzed as unknown together with the samples. Abbreviations: r.z, reaction zone; h.r., host rock; n.a., not applicable; ol, olivine; opx, orthopyroxene; cpx, clinopyroxene; amph, amphibole.
[b]Mg# = Mg/(Mg + Fe) atomic ratio.

study (spinel harzburgites) were collected in recent andesitic tephras, together with those reported by *Ionov* [2010] and have generally similar major and trace element compositions. The samples in this study contain thin (≤5 mm), opx-rich veins (Figures 1b and 1c). Representative major element data for vein minerals are given in Table 1.

[8] Type A veins show no petrographic evidence of significant melt-host reaction (Figure 1b); they are >0.5 mm thick and consist almost entirely of Fe-zoned opx ($Wo_{0–5}$-$En_{89–92}$-$Fs_{6–8}$), with rare (<1%) cpx ($Wo_{46–48}$-$En_{48–51}$-$Fs_{3–4}$) and (Ti, Na, K)-poor amphibole (pargasite) found as small (<100 μm) aggregates also including empty vesicles.

[9] Type B veins have irregular margins (Figure 1c) and common reaction zones (Figure 2a); they are grouped into "thick" (Type B1, >0.5 mm) and "thin" (Type B2, <0.5 mm) (Figures 1c and 2b).

Table 2. Trace Element (ppm) Analyses of Bulk Type A Veins With BIR-1 Standard and Analytical Blank[a]

	Av21-2 (1:1963)	Av21-2bis (1:2018)	Av21-3 (1:1968)	Av21-3bis (1:1884)	Av20 (1:2092)	Av20bis (1:1490)	Av20ter (1:1996)	BIR-1 (1:2527)	Blank (n.a.)
Li (ppm)	0.743	0.846	0.859	0.827	0.946	0.967	0.931	3.00	0.041
Rb	0.12	0.15	0.11	0.12	0.20	0.21	0.20	0.29	0.01
Sr	2.21	2.41	2.42	2.46	0.84	0.92	0.92	109	0.023
Y	0.665	0.785	0.628	0.632	0.373	0.403	0.394	15	0.001
Zr	0.331	0.277	0.260	0.243	0.209	0.200	0.259	19	0.023
Nb	0.026	0.020	0.022	0.024	0.024	0.027	0.029	0.577	0.004
Cs	0.006	0.007	0.005	0.005	0.008	0.008	0.008	0.009	0.001
Ba	4.45	5.64	2.14	2.33	4.36	4.70	4.59	6.92	0.05
La	0.0801	0.0942	0.0968	0.101	0.0720	0.0755	0.0775	0.6174	0.0017
Ce	0.255	0.289	0.301	0.308	0.189	0.197	0.199	1.89	0.0010
Pr	0.039	0.045	0.051	0.052	0.031	0.033	0.033	0.352	0.0002
Nd	0.200	0.231	0.259	0.269	0.157	0.171	0.169	2.34	0.0005
Sm	0.063	0.074	0.084	0.087	0.050	0.055	0.055	1.04	0.0003
Eu	0.0195	0.022	0.024	0.024	0.0141	0.0151	0.0152	0.508	0.0002
Gd	0.071	0.082	0.086	0.087	0.052	0.057	0.054	1.78	0.0002
Tb	0.0140	0.0163	0.0174	0.0172	0.0104	0.0114	0.0113	0.356	0.00004
Dy	0.104	0.119	0.131	0.128	0.077	0.087	0.083	2.64	0.0001
Ho	0.022	0.025	0.027	0.027	0.0160	0.0176	0.0171	0.581	0.00003
Er	0.068	0.077	0.082	0.082	0.050	0.054	0.053	1.65	0.0001
Tm	0.0112	0.0130	0.0142	0.0140	0.0083	0.0092	0.0088	0.241	0.00003
Yb	0.083	0.095	0.105	0.106	0.063	0.071	0.068	1.60	0.00002
Lu	0.0148	0.0169	0.0187	0.0186	0.0110	0.0123	0.0117	0.261	0.00002
Hf	0.0085	0.0084	0.0084	0.0078	0.0056	0.0054	0.0064	0.608	0.0005
Ta	0.0040	0.0036	0.0048	0.0045	0.0038	0.0079	0.0031	0.065	0.0018
Pb	0.213	0.271	0.191	0.180	0.361	0.338	0.397	3.22	0.056
Th	0.0174	0.0198	0.024	0.025	0.0183	0.0186	0.0178	0.033	0.0002
U	0.020	0.025	0.0090	0.0093	0.0092	0.0094	0.0093	0.0144	0.0001

[a]Samples Av21-2, Av21-2bis, Av21-3 and Av21-3bis are different parts of a single Type A vein crosscutting harzburgite Av21, while samples Av20, Av20bis and Av20ter come from harzburgite Av20. BIR-1 standard was measured during the same run as Type A vein samples. Numbers in parentheses in the header row are dilution factors of the samples (n.a. indicates not applicable).

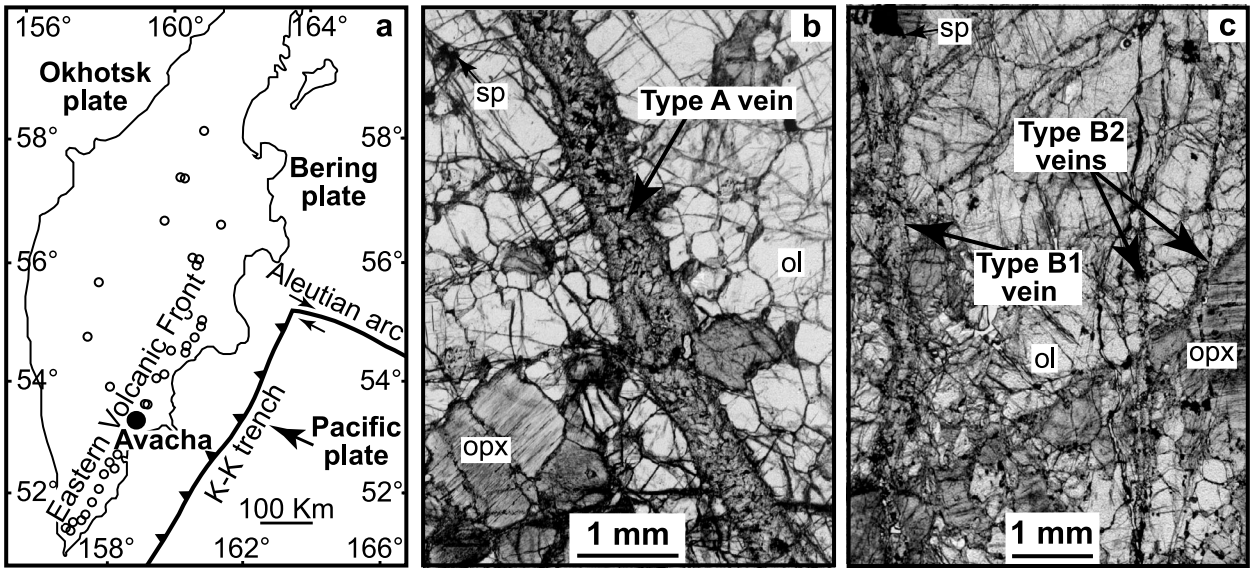

Figure 1. (a) Location map of the Avacha volcano with major tectonic and volcanic zones of the Kamchatka peninsula (NE Russia); K-K trench, Kurile-Kamchatka trench. (b, c) Photomicrographs of polished sections (120 μm) in transmitted light; ol, olivine; opx, orthopyroxene; sp, spinel. Figure 1b is a xenolith cut by a Type A vein; Figure 1c is a xenolith cut by Type B1 and B2 veins.

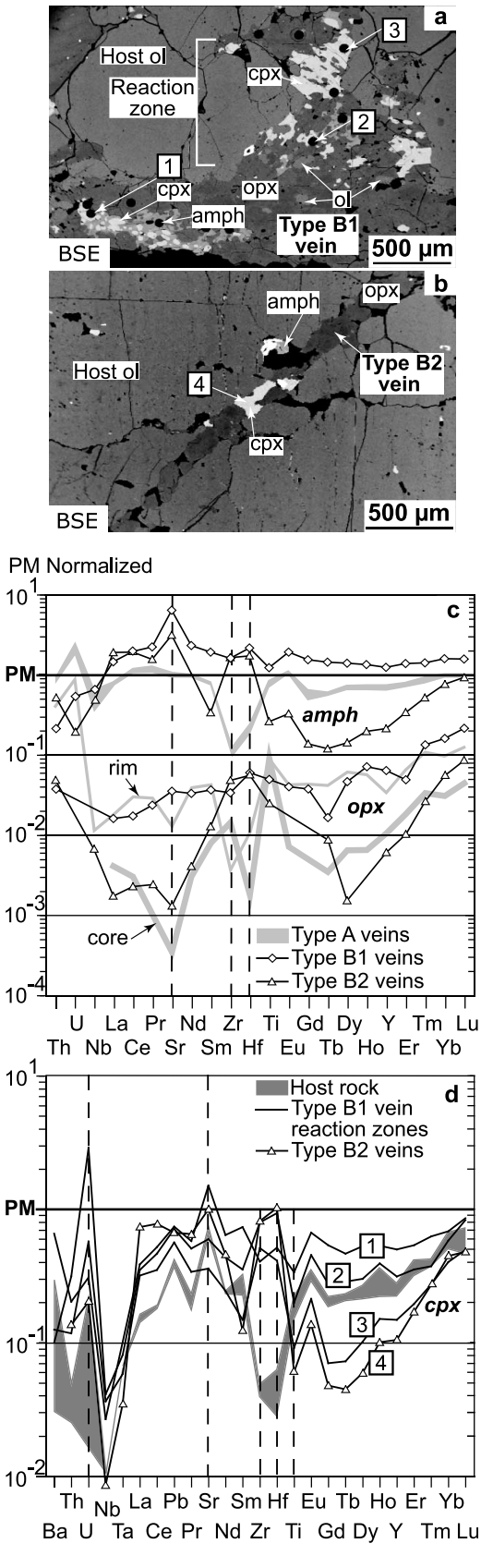

Type B1 veins have minor amounts of olivine (<10%, Figure 2a), which contains more Fe (Fo_{89}) and less Ni (~0.2 wt.% NiO) than olivine in the host harzburgite xenoliths (Fo_{90} and ~0.4 wt.% NiO reported by *Ionov* [2010]). Amphibole and cpx occur near vein centers and in reaction zones (Figure 2a) and are more common than in Type A veins. Pyroxenes and amphiboles have lower Mg# (e.g., opx with $Wo_{0–2}$-$En_{88–90}$-$Fs_{9–10}$) and higher Al_2O_3 (up to ~3 wt.% in opx and 11 wt.% in amphibole) and Na_2O (>2 wt.% in amphibole) than in Type A veins (Table 1).

4. Trace Element Variability in the Veins

[10] Representative trace element data for vein minerals are given in Table 1 and illustrated in Figure 2. Opx cores in Type A veins have low HREE (Lu ~1 ppb) relative to primitive mantle (PM [*McDonough and Sun*, 1995]) estimates and show a continuous decrease in PM-normalized abundances from HREE to LREE. Importantly, cores of opx in Type A veins have high $(Zr/Sm)_N$ (~2) and $(Zr/Hf)_N$ (~8) where N refers to PM-normalized abundances (Figure 2c). Opx in Type A veins have 4–13 times higher MREE and LREE in their rims than in their cores. Opx rims in Type A veins have distinctive pronounced negative Zr and Hf anomalies with $(Zr/Hf)_N < 1$ and high Th and U. Type A vein amphiboles have negative Zr and Hf anomalies mirroring those in opx rims, mildly sinusoidal REE patterns and high LILE (Figure 2c).

[11] Minerals in the centers of Type B1 veins share important similarities with those of Type A veins, notably almost identical REE abundances in opx rims, but two important points are different: (1) 2–3 times higher REE abundances in amphibole at similarly flat REE patterns and (2) no negative Zr and Hf anomalies in pyroxenes and amphiboles (Figure 2c).

[12] Trace element patterns of minerals in Type B2 veins are distinct from those in both Type A and B1

Figure 2. Backscattered electron (BSE) images of (a) a reaction zone between a Type B1 vein and host Avacha harzburgite and (b) a Type B2 vein; cpx, clinopyroxene; amph, amphibole, other abbreviations are as in Figure 1. PM-normalized [*McDonough and Sun*, 1995] trace element abundance patterns in (c) opx and amphibole from Type A and B veins and (d) cpx from Type B veins, reaction zones and host Avacha harzburgite. Numbers in Figures 2a, 2b, and 2d indicate laser pits produced during LA-ICPMS trace element analyses.

veins. Minerals in Type B2 veins have lower HREE than in Type B1 veins, low $MREE_N$ relative to $LREE_N$ and $HREE_N$ (U-shaped REE patterns, e.g., $[La/Tb]_N \sim 10$ in amphiboles) whereas the Zr and Hf abundances are close to those in Type B1 veins (Figure 2c).

[13] Trace element patterns of minerals are highly variable in reaction zones adjacent to Type B1 veins. Abundances of HREE and MREE in cpx from Type B1 veins progressively decrease from laser pit 1 (vein center) to pit 3 (reaction zone) in Figure 2d while La, Zr and Hf do not vary significantly. Importantly, patterns of cpx in spot 3 are close to those for cpx in Type B2 veins (Figures 2b and 2d, spot 4), but with lower abundances of most incompatible REE (La and Ce).

5. Vein Crystallization Modeling

[14] Below, the word "initial" is used to typify the most primitive and original melt intruding Avacha peridotites (i.e., unaffected by reaction processes with the host rock), while "parental" is used to characterize the different melts that crystallize each vein types (i.e., affected or not by reaction processes with the host rock). We model the compositions of parental melts for Type B1 and B2 veins based on major and trace element abundances in their minerals, assuming that they are in chemical equilibrium. For this purpose, we run equilibrium crystallization of a melt with the "adiabat_1ph" program [*Smith and Asimow*, 2005] and "pMELTS" thermodynamic algorithm [*Ghiorso et al.*, 2002]. The melt is set in an initial super-liquidus state and the modeling is run at isobaric conditions suitable for the mantle wedge (1.5 GPa). The liquid line of descent in the lithospheric mantle is likely to be controlled by the temperature and oxygen fugacity (fO_2) of wall rock peridotites reported earlier by *Ionov* [2010]. Accordingly, the crystallization is run at the Fayalite-Magnetite-Quartz (FMQ) buffer until temperature drops to 900°C. Mineral/melt partition coefficients for trace elements ($D_i^{crystal/melt}$ where i is the chemical element of interest) were assumed constant during crystallization; they are given and referenced in Table S1 in the auxiliary material.[1] H_2O is presumed to reside only in the melt until saturation is reached.

[15] First, major element composition of the initial melt was constrained with several modeling runs using a range of appropriate starting compositions. Our preferred composition matches best the modal abundances and major element compositions of Type B veins (see section 4) considered to be the latest crystallization products of the liquid: $SiO_2 \sim 54$ wt.%, MgO∼31 wt.%, ∼6.5 wt.% FeO_{tot}, 1.5–1.7 wt.% CaO and Al_2O_3, 0.15–0.25 wt.% of TiO_2 and Na_2O and $H_2O \sim 5$ wt.%. The modeling shows that the liquidus phase near 1400°C is a highly magnesian olivine (Mg#∼0.94). As crystallization proceeds, olivine is first joined by opx with Mg# decreasing from 0.93 to 0.90 between 1300 and 1100°C, followed by cpx (Mg#∼0.91) at 1000–900°C and amphibole (Mg#∼0.92) at 900°C. Mineral proportions and major element contents at the late crystallization stages (1100–900°C) correctly reproduce those of Type B veins (Table S1). Thermodynamic data derived from the pMELTS algorithm indicate that H_2O activity (a_{H_2O}) in the melt increases from 0.39 at 1400°C to 1 at 1100°C when H_2O saturation in the melt is attained (Table S1).

[16] Using the major element composition constrained above, trace element abundances of the parental melts of Type B1 and B2 veins were fitted with several modeling runs in order to reproduce trace element abundances in the vein minerals (see section 4). Distinct trace element compositions are required to reproduce the compositions of Type B1 and B2 veins (Figures 3a and 3b). The parental melt inferred to reproduce Type B1 veins has a nearly flat REE pattern at 0.1 x PM values, slightly enriched in HREE relative to LREE-MREE, with Sr, Rb and Ba spikes and low Nb and Ta (Figure 3a). The parental melt for Type B2 veins has a U-shaped REE pattern and Zr-Hf spikes (Figure 3b). Trace element compositions of all minerals (opx, cpx and amph) in the inner parts of Type B veins are correctly reproduced with these two parental melt compositions at 1000–900°C (Figures 3c and 3d). Importantly, measured trace element abundances in cores of opx in Type A veins match those in opx modeled at 1200–1100°C using the parental melt for Type B1 veins (Figure 3c). Minor differences between modeled and analyzed trace element abundances in the opx from Type B veins concern Rb, Ba and Sr and may be related to uncertainties of $D^{opx/melt}$ used in the modeling and/or high concentrations of these elements in micro-inclusions and cracks in the opx. Complete modeling results are given in Table S1 in the auxiliary material.

[17] Four main inferences can be drawn based on the crystallization modeling. (1) All minerals in Type B veins are in trace element equilibrium. Their trace element budgets are controlled by their

[1] Auxiliary materials are available in the HTML. doi:10.1029/2012GC004145.

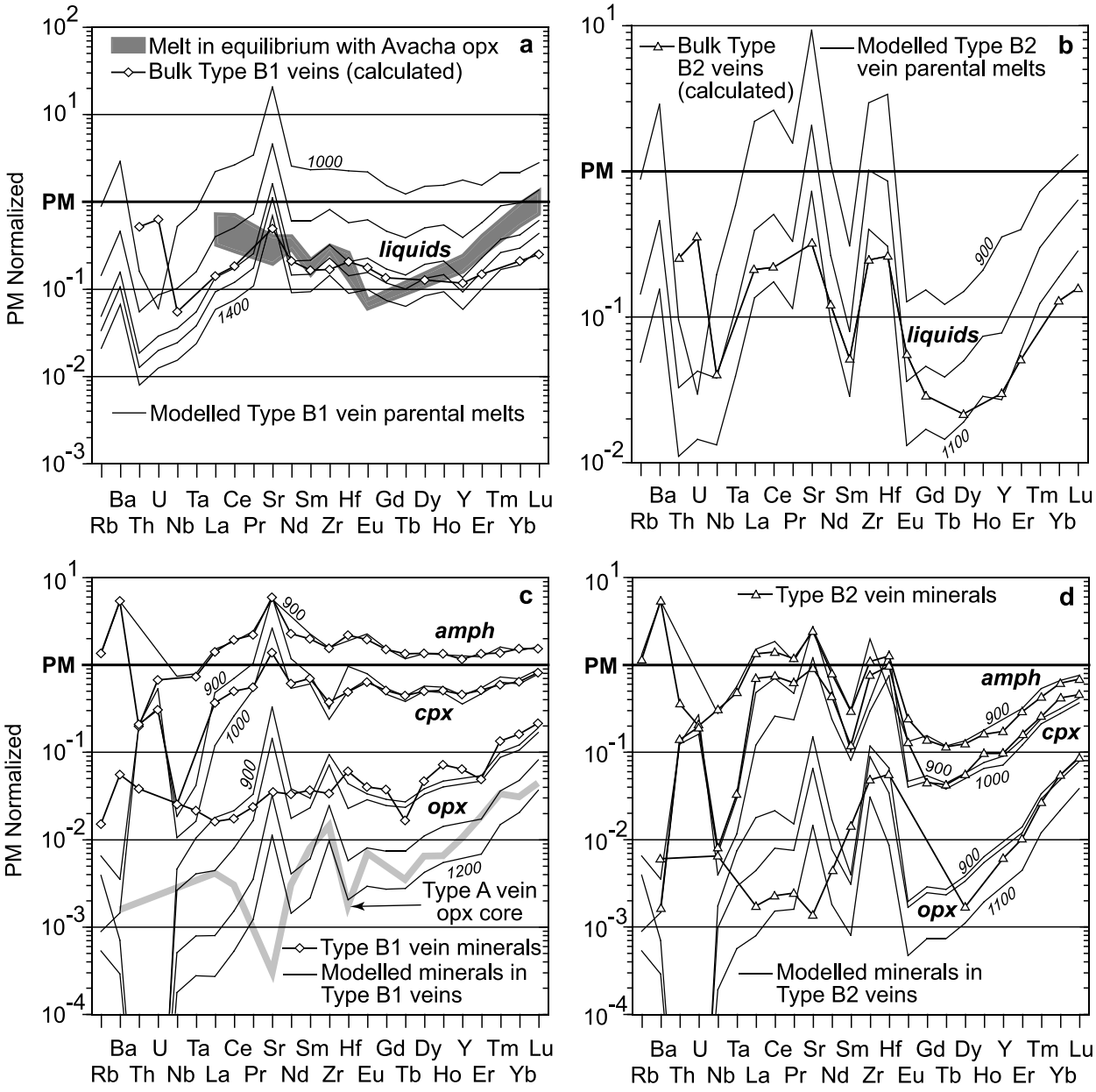

Figure 3. Comparison between modeled (pMELTS) and analyzed or calculated trace element abundance patterns of Avacha veins (PM-normalized after *McDonough and Sun* [1995]). Calculated bulk veins and modeled parental melts for (a) Type B1 and (b) B2 veins. Analyzed and modeled minerals for (c) Type B1 and (d) B2 veins. Temperatures (in degrees Celsius) obtained from the pMELTS modeling are indicated in italics. Also shown in Figure 3a is the compositional range calculated for hypothetical melts in equilibrium with the most metasomatized opx in Avacha harzburgites from *Ionov* [2010] (dark-gray field). Abbreviations and symbols are the same as in Figures 1 and 2.

parental melts and do not result from $D_i^{crystal/melt}$ variations during crystallization or sub-solidus re-equilibration. (2) Major element compositions of parental melts inferred for Type B1 and B2 veins are similar. (3) The parental melt for Type B1 veins forms opx at high temperature (1200–1100°C), with trace element patterns similar to those in cores of opx from Type A veins (Figure 3b). (4) Amphibole in Type A veins, which has distinctive negative Zr-Hf anomalies, is not in trace element equilibrium with cores of coexisting opx, but appears to be equilibrated with their rims. The parental melt

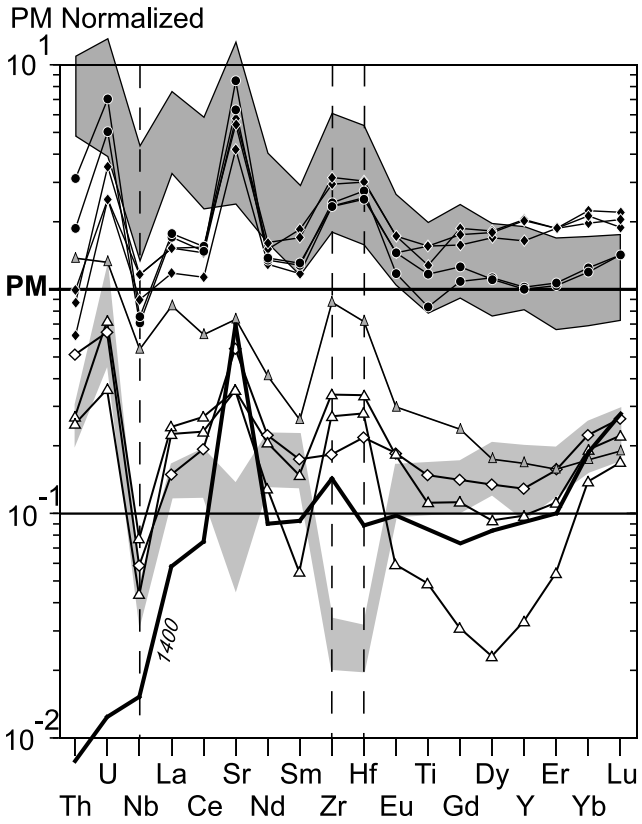

Figure 4. Comparison of PM-normalized [*McDonough and Sun*, 1995] trace element abundance patterns for: solution ICPMS analyses of bulk Type A veins (light-gray field), calculated bulk compositions of Type B1 (white diamond) and B2 veins (white triangle) and pMELTS-modeled initial liquid with temperature in degrees Celsius (thick black pattern). Also shown are literature data on Cape Vogel LCB lavas (dark-gray field) [*König et al.*, 2010] and their most depleted primary melts from spinel-hosted inclusions by *Kamenetsky et al.* [2002] (gray triangle), "transitional" lavas (black diamond) and LCB (black circle) from the Mariana fore-arc reported by *Reagan et al.* [2010].

obtained for Type B1 veins by both major and trace element modeling is referred to as "modeled initial liquid" in the following text.

6. Trace Element Compositions of Bulk Veins

[18] Solution ICPMS analyses of Type A veins are presented in Table 2 and shown in Figure 4. The patterns of bulk Type A veins are very similar to those of opx rims and amphiboles in these veins, i.e., flat REE at low abundances (0.2–0.3 times PM values), negative high field strength element [HFSE] anomalies (notably Zr-Hf) and LILE spikes (Figure 4). We conclude that the bulk Zr-Hf abundances of Type A veins are controlled by opx rims and amphiboles, which are not in chemical equilibrium with the opx cores that formed earlier (see section 5).

[19] Solution and laser ablation ICPMS analyses of Type A veins and their minerals were used to calculate modal abundances of opx, cpx and amphibole in these veins. These modal estimates are also used here to calculate trace element abundances of bulk Type B veins, which are shown in Table 3. The cpx and amphibole abundances calculated for the Type A veins are the best estimates for Type B veins as well because their modal compositions are highly variable on mm scale (e.g., Figure 2a) and cannot be assessed from vein images. The modal estimates based on Type A veins are the only means to compare directly the measurement-based calculations and our pMELTS modeling. The calculated bulk abundances are similar to those in the modeled parental melts produced at 1200°C and 1100°C by pMELTS modeling for Type B1 and B2 veins, respectively (Figures 3a and 3b). Th and U abundances in calculated bulk veins are higher than in the modeled melts and may result from higher

Table 3. Calculated Bulk Veins[a]

	Modal%: opx: 82%; cpx: 10%; amph: 8%[b]		
	Vein Type B1	Vein Type B1-r.z.[c]	Vein Type B2
Ti (ppm)	157	118	52
Sr	9.67	6.30	6.30
Y	0.496	0.377	0.127
Zr	1.74	3.21	2.57
Nb	0.035	0.047	0.026
La	0.0896	0.146	0.136
Ce	0.303	0.420	0.363
Nd	0.259	0.239	0.150
Sm	0.066	0.056	0.021
Eu	0.027	0.026	0.0085
Gd	0.071	0.056	0.0155
Dy	0.084	0.058	0.0144
Er	0.063	0.045	0.022
Yb	0.091	0.078	0.056
Lu	0.0166	0.0139	0.0105
Hf	0.057	0.088	0.073
Pb	0.071	0.040	0.037
Th	0.040	0.021	0.0198
U	0.0126	0.0141	0.0070

[a]Bulk veins were estimated with individual LA-ICPMS analyses of vein minerals and modal proportions calculated by least square regression from Sol-ICPMS and LA-ICPMS analyses of Type A veins and their minerals.
[b]Abbreviations: opx, orthopyroxene; cpx, clinopyroxene; amph, amphibole.
[c]Abbreviation: r.z., reaction zone.

calculated modal cpx and amphibole than those modeled with pMELTS (see Tables 3 and S1).

7. Discussion

7.1. Melt Fractionation and Interaction Processes

[20] Strong negative Zr-Hf anomalies are only present in the latest materials (opx rims and amphiboles) to crystallize in Type A veins (Figure 2c). Petrographic data on Type A veins suggest little interaction with the host peridotites, thus Type A veins can be viewed as closed systems. Late-stage evolution (1000–900°C, i.e., host peridotite equilibration temperature [*Ionov*, 2010]) of the melt in Type A vein conduits represents massive opx fractionation (~90%, Table S1). First, the opx fractionation can significantly deplete the residual liquid in Zr-Hf relative to MREE, because $D_{Zr,Hf}^{opx/melt} \geq D_{MREE}^{opx/melt}$ have been reported in high-P experiments on element partitioning [e.g., *Green et al.*, 2000]. Second, massive fractionation of nominally anhydrous opx likely produces a residual, hydrous fluid-rich melt (or supercritical liquid), with a major element composition close to that of andesites when re-calculated on anhydrous basis (see the melt produced at 1000°C during pMELTS modeling in Table S1). Experimental data show that an aqueous fluid can be exsolved from andesitic melts at 1000–900°C and ~1.2 GPa [*Kawamoto*, 2006, and references therein]. Aqueous fluid exsolution is indicated by the occurrence of amphibole exclusively in isolated vesicle-rich aggregates in Type A veins (Table S1). On the other hand, pMELTS modeling indicates a substantial increase of a_{H_2O} in the melt during opx fractionation, which leads to fluid (pure H_2O in the model) saturation below 1100°C (Table S1). Experimental partition coefficients for melt/hydrous fluid ($D_i^{melt/fluid}$) are ≫1 for Zr and Hf but much lower for MREE at 900–1000°C and 2 GPa [*Ayers et al.*, 1997; *Brenan et al.*, 1995; *Keppler*, 1996]. Hence, distinctive Zr-Hf negative anomalies in opx rims of Type A veins and amphiboles likely reflect late-stage evolution of the liquid caused by massive opx fractionation and possibly by a related a_{H_2O} increase. It follows that these Zr-Hf negative anomalies are a result of fractional crystallization and not a signature of the initial liquid of Type A veins.

[21] Late-stage minerals are more common and have lower Mg# and higher Al, Na and REE in Type B1 veins than in Type A veins (Table 1 and Figure 2c). Anhydrous to hydrous mineral assemblages in metasomatic veins and host peridotites may result from continuous differentiation of a single initial melt during its percolation as indicated by experimental work [*Pilet et al.*, 2010] and data on mantle peridotites [*Ionov et al.*, 2006]. Crystallization modeling shows that the parental liquids inferred for Type B1 veins can produce high-temperature opx (1200–1100°C), which is similar in major and trace element composition to opx cores in Type A veins (Figure 3c). The modeling indicates a continuous differentiation process (combined with increasing a_{H_2O}), with progressive enrichment in incompatible elements in a unique initial melt to produce first Type A and then Type B1 veins (Table S1). We conclude that Type B1 veins crystallized from fractionated, hydrous derivates of melts forming Type A veins.

[22] Trace element variability in reaction zones adjacent to Type B1 veins is the key to understand their links to Type B2 veins (Figure 2d). The process that formed U-shaped REE patterns in the reaction zones (Figures 2a and 2c) produced only minor changes in Zr and Hf abundances to yield patterns that mimic those in Type B2 veins (Figure 2d). Olivine in host rocks has much lower MREE, LREE and Zr-Hf than HREE [*Ionov*,

2010]; some olivine in the reaction zones may be relics of the host peridotite following its partial assimilation. We attribute the formation of the U-shaped REE patterns to progressive re-equilibration of the melt with the host olivine, possibly accompanied by fluid-assisted peritectic reaction of the olivine with the Si-rich melt in the reaction zones:

$$\text{olivine} + SiO_2 - \text{rich melt}_1 \rightarrow \text{orthopyroxene} + \text{melt}_2$$

at decreasing liquid mass [*Müntener et al.*, 2001]. HREE-MREE in the reacted melt ($melt_2$) are buffered by the host mantle while the abundances of the highly incompatible LREE, which reside in the reacted melt, increase. The REE-decoupling resembles that predicted for chromatographic processes, which may produce similar U-shaped REE patterns [*Bodinier et al.*, 1990]. Such a process is difficult to model based on mineral compositions in reaction zones of Type B1 veins because they are highly variable on a small scale suggesting the lack of chemical equilibrium. On the other hand, crystallization modeling shows that trace element patterns of parental melts for Type B2 veins must have been modified through a process similar to that recorded in reaction zones (Figures 3b and 3d). It follows that percolation of the modeled initial liquid in peridotites may lead to a complete modification of its trace element signatures at low melt/wall rock ratios.

7.2. An Alternative Model for Low-Ca Boninite Petrogenesis

[23] Calculated bulk trace element abundances of Type B veins are compared in Figure 4 to the modeled initial liquid, solution ICPMS data on Type A veins as well as recent literature data on LCB. The estimates for bulk Type B veins share the distinctive patterns of worldwide LCB, in particular their range of enrichments in LREE relative to MREE-HREE with ubiquitous Zr-Hf spikes, as shown in Figure 4 for the Mariana fore-arc (transitional lavas and LCB in *Reagan et al.* [2010]), the Bonin Islands and Mariana trench and the Cape Vogel LCB lavas. Bulk Type B2 veins with strongly U-shaped REE patterns mimic some LCB from Chichijima (Bonin Islands) [*Pearce et al.*, 1999; *Taylor et al.*, 1994]. Importantly, all the Avacha bulk veins and the modeled initial liquid have HREE abundances that match those of the most depleted liquid reported by *Kamenetsky et al.* [2002] for spinel-hosted melt inclusions from Cape Vogel LCB. The similarities in HREE abundances suggest that the Cape Vogel LCB and the modeled initial liquid may derive from similar mantle sources (see section 7.3.2.).

[24] If the Type B vein patterns mimic those of most LCB worldwide (Figure 4), they appear to be the result of a process distinct from those previously proposed for all LCB magmas; these alternative models are discussed below.

[25] Slab melts may selectively mobilize some HFSE [*Klemme et al.*, 2002] and have been recently inferred to be responsible for Zr-Hf spikes in Cape Vogel LCB [*König et al.*, 2010]. However, some of the arguments for a slab-melt component, e.g., high $(Gd/Yb)_N$ or low ε_{Nd} and ε_{Hf} [*König et al.*, 2010], do not apply to other LCB such as those from the Mariana arc [*Pearce et al.*, 1999; *Reagan et al.*, 2010]. The LCB from the Mariana arc have U-shaped REE patterns and Zr-Hf spikes (Figure 4) in combination with Nd-Hf isotopic compositions typical of mid-ocean ridge basalts (MORB) [*Pearce et al.*, 1999; *Reagan et al.*, 2010]. In the case of the Avacha veins, slab-melt affinity is also hard to reconcile with low $(Th/U)_N$ (~0.7), high $(Ba/Nb)_N$ (up to 5) and $(LREE/MREE)_N < 1$ (see experimental results at 1000°C and 4 GPa of *Kessel et al.* [2005]) in the modeled initial liquid (Figures 3a and 4). Furthermore, thermal modeling of the south Kamchatka mantle wedge [e.g., *Manea et al.*, 2005] and geochemical data on erupted magmas [e.g., *Duggen et al.*, 2007] argue against slab melting below the arc front and support metasomatism of the mantle wedge by slab fluids. Our modeling suggests that the parental melts of Type B2 veins have Zr-Hf spikes (Figures 2c, 2d, 3b and 4) but strong Zr-Hf enrichments relative to MREE are not a feature of any previously proposed slab-derived aqueous or supercritical fluid [e.g., *Brenan et al.*, 1994; *Kessel et al.*, 2005]. We conclude that Zr-Hf "enrichments" over MREE observed in erupted LCB, like in Type B2 veins, may not result from the addition of a metasomatic component to their melting source.

[26] LCB magmas have $(La/Sm)_N$ up to 3 (e.g., Cape Vogel LCB reported by *Kamenetsky et al.* [2002] and shown in Figure 4). It follows, assuming a metasomatic origin for their U-shaped REE patterns and using experimental $D_{La,Sm}^{opx/melt}$ [*Gaetani et al.*, 2003; *McDade et al.*, 2003] and $D_{La,Sm}^{peridotite/fluid}$ [*Ayers et al.*, 1997], that slab-derived metasomatic fluids in equilibrium with mantle opx in the LCB melting source had similar $(La/Sm)_N$. Such high $(La/Sm)_N$ can be generated in the melting source of LCB as shown by experiments on fluids in equilibrium with an eclogitic MORB at 700–900°C and

4 GPa [*Kessel et al.*, 2005], which produced LREE-rich metasomatic agents (e.g., aqueous fluid) with $(La/Sm)_N$ ranging from 7 to 20. On the other hand, U-shaped REE patterns with high $(La/Sm)_N$, like those in our samples, may form by chromatographic reactive porous flow of melt through residual peridotites [*Bodinier and Godard*, 2003] and are very common in fore-arc and ophiolite peridotites [e.g., *Parkinson and Pearce*, 1998]. It follows from the data on reaction zones of Type B1 veins (Figure 2d) that U-shaped REE patterns with Zr-Hf spikes in LCB may not be formed during the generation of their primary magmas.

[27] To sum up, our results suggest that the degrees of "enrichment" of Zr-Hf relative to MREE, and of LREE relative to MREE-HREE, in LCB magmas may not be related exclusively to the overprint of a unique slab component on their mantle source, contrary to what has been proposed in numerous earlier studies [*Hickey and Frey*, 1982; *König et al.*, 2010]. We put forward a new model for LCB petrogenesis, which does not involve a (LREE, Zr, Hf)-rich slab component, and argue that the relative Zr-Hf "enrichments" in these magmas may be generated through melt fractionation and interaction along a continuous liquid line of descent during its ascent in the mantle wedge above the melting zone. The model of fractionation and reactive percolation proposed here could also account for the broad magnitude of Zr-Hf "enrichments" (or more likely MREE-HREE depletions) found in LCB [e.g., *Hickey and Frey*, 1982; *Taylor et al.*, 1994] without invoking complex melt source heterogeneities. In our model, the shape and scale of the MREE-HREE depletion, controlling in turn those of Zr-Hf spikes, are mainly constrained by the type of mantle rocks percolated by an initial LCB melt during its ascent and by percolation distance.

7.3. Inferences for Initial Liquid, Mantle Source, Metasomatic Component and Geological Setting of Low-Ca Boninites

7.3.1. Initial Liquid

[28] If our model is correct (see section 7.2.), Type A and Type B1 veins crystallized from an initial LCB liquid, which reacted only slightly with the host mantle. Initial MgO estimates from primitive, spinel-hosted, melt inclusions in LCB from Cape Vogel yield values similar to that of the modeled initial liquid in the most Mg-rich primary LCB liquid (30.4 wt.% MgO in sample 6A-9 from *Kamenetsky et al.* [2002]). Furthermore, the modeled initial liquid produces liquidus olivine at 1400°C with high Mg# (0.94, Table S1) matching those identified in erupted LCB [e.g., *Walker and Cameron*, 1983]. The refractory major element composition of the modeled initial liquid (low Ca, Al, Ti and alkalis) is in line with published data on bulk rock and mineral compositions of LCB [*Walker and Cameron*, 1983]. The only significant difference between the modeled initial liquid and the melt inclusion in sample 6A-9 reported by *Kamenetsky et al.* [2002] is lower Al_2O_3 (1.7 versus 4.3 wt.%). Significant Al exchange between melt inclusions and host spinel was recently reported by *Ionov et al.* [2011], and such a process may have also affected the compositions reported by *Kamenetsky et al.* [2002]. Finally, we used ~5 wt.% H_2O in the modeled initial liquid, which is above estimates of *Kamenetsky et al.* [2002] (~3 wt.%) for the Cape Vogel LCB melt inclusions.

[29] The trace element pattern of the modeled initial liquid is similar to those of typical island arc tholeiites. This suggests that the LCB may be produced at late stages of melting events that initially generate island arc tholeiites in the mantle wedge, as previously inferred from close field associations of these two rock types [*Cameron*, 1989; *Crawford and Keays*, 1987]. However, our model differs from those put forward previously in that it implies no significant evolution of trace element signatures of the slab-derived metasomatic components during the transition from island arc tholeiites to LCB (see section 7.3.3.).

7.3.2. Mantle Source

[30] Type A and B veins have fine-grained, magmatic textures and are likely to record a recent magmatic event, which took place shortly before the entrainment of the Avacha harzburgites in host magma. Hence, the latest equilibration conditions of the Avacha xenoliths may give important information on the mantle source of the modeled initial liquid.

[31] The Avacha veins are opx-rich (exceeding 90% in Type A veins), in line with the formation of LCB mainly through opx fractionation [*Jenner*, 1981] and/or accumulation [*König et al.*, 2010]. The opx-rich veins may be produced by crystallization of a melt with a primitive opx-rich composition at ≥1400°C and relatively high pressure (≥1.5 GPa), according to MgO-SiO_2 phase relationships [*Thompson et al.*, 2007] and our pMELTS modeling. This is consistent with melting at high temperature (≥1400°C), as previously inferred from LCB studies [e.g., *Kamenetsky et al.*, 2002], though

the relatively high pressure of LCB melt generation indicated by our results, differs significantly from previous estimates (e.g. <1 GPa by *Walker and Cameron* [1983]). A high pressure (≥1.5 GPa) for the formation of Avacha veins is consistent with available major element data on (1) the host bulk xenoliths, which constrain the depth of formation of their refractory protolith by flux-melting and (2) the minerals in the host xenoliths, which yield thermo-barometric estimates of their final equilibration conditions [*Ionov*, 2010].

[32] The major element composition of the modeled initial liquid suggests that the mantle source is a refractory, cpx-free harzburgite like those from Avacha [*Ionov*, 2010]. Recent modeling [*Parman and Grove*, 2004] and experiments [*Falloon and Danyushevsky*, 2000] on harzburgite hydrous melting suggest that melts produced at 1500°C and below 2 GPa can contain up to ~27 wt% MgO and ~54 wt.% SiO_2. However, the melting experiments of *Falloon and Danyushevsky* [2000] were performed with lower H_2O in the melts produced (≤2 wt.%) than in our modeled initial liquid. On the other hand, low HREE abundances in the modeled initial liquid suggest that the liquid was generated from a more depleted mantle source than those proposed for MORB (Figure 3a and 4).

[33] We calculate the range of trace element compositions of theoretical melts in equilibrium with the most metasomatized opx in the Avacha harzburgites studied by *Ionov* [2010] (e.g., sample Av11) using $D_i^{opx/melt}$ determined in peridotite melting experiments at mantle wedge conditions [*McDade et al.*, 2003]. Importantly, the calculated melt has a trace element pattern similar to that of the modeled initial liquid. If our fractionation and reaction model is correct, the initial melt of LCB may be derived from highly refractory harzburgites similar to fore-arc peridotites [e.g., *Parkinson and Pearce*, 1998], which are characterized by higher opx and SiO_2 and lower cpx, Al_2O_3 and CaO abundances than refractory peridotites in other tectonic settings [*Ionov*, 2010]. These features can result from high degrees (30–35%) of melting induced by silica-rich fluids, inferred to occur at ~1.5 GPa, and which produced island arc basaltic magmas [*Ionov*, 2010; *Soustelle et al.*, 2010]. Such a refractory source implies that melting phase relationships for LCB may be controlled by low-Al opx at ≥1.5 GPa (see the evidence for pressure conditions of flux-melting in *Ionov* [2010]) that could explain the unusual major element composition of LCB initial melt such as high SiO_2 (Table S1). In turn, high SiO_2 in the produced melt will enhance reaction of this melt with mantle olivine during ascent above the melting zone (see section 7.1.).

7.3.3. Metasomatic Component and Geological Setting

[34] The modeled initial liquid of Type A and B1 veins has flat LREE-MREE patterns, low Nb and Ta and high LILE abundances (Figure 3a). These features are consistent with the widely accepted, "classical" trace element signatures of metasomatic agents proposed for subduction zones [*Keppler*, 1996; *Kessel et al.*, 2005]. Niobium depletion and high LILE in the modeled initial liquid are likely to be related to fluxing by slab-derived silica-rich fluids generated in equilibrium with residual, refractory eclogitic phases [e.g., rutile, *Brenan et al.*, 1994]. Silica-rich fluids can be produced at depths down to 100 km [*Bureau and Keppler*, 1999, and references therein] and are in good agreement with the "cold" south Kamchatka subduction geotherm [e.g., *Manea et al.*, 2005]. On the other hand, slab-related melts would require unusually high temperature at the slab-mantle interface (≥1000°C [*Kessel et al.*, 2005]).

[35] *Cameron et al.* [1979] concluded that LCB can only occur in a fore-arc setting with subduction initiation along spreading centers. Ridge subduction [*Crawford and Keays*, 1987], oceanic subduction underneath a hot lithosphere [*Crawford et al.*, 1989] and slab rollback extension [*Bédard*, 1999] were also proposed as LCB geological settings. The occurrence of high temperature melts, like those of LCB, inferred in this study to be present in the mantle beneath the mature southern Kamchatka arc, may indicate that this type of magmas is much more widespread than previously thought and may be generated at different stages of arc formation. It may explain some complex field relations observed for these magmas, such as when they overlie andesites [*Crawford and Keays*, 1987].

8. Conclusions

[36] Spinel harzburgites from Avacha contain opx-rich veins of mantle origin. Veins that do not react with the host harzburgites have LREE-depleted to flat REE patterns, high LILE abundances, Nb negative anomalies and no Zr-Hf anomalies. Veins reacting with the host harzburgites have U-shaped REE patterns with Zr-Hf spikes, which mimic trace element signatures of LCB.

[37] Major and trace element modeling indicate that all veins formed from an MgO-rich (~30 wt.%) and silicic (~54 wt.% SiO_2) initial liquid, strongly

depleted in incompatible elements (Al_2O_3, TiO_2 and alkalis) and with trace element signatures similar to those of typical island arc tholeiites. This liquid experienced strong fractionation in the mantle wedge lithosphere.

[38] Trace element signatures of LCB magmas (U-shaped REE patterns and Zr-Hf spikes) may be produced by a combination of strong melt fractionation and reaction with mantle rocks above the source regions of their initial liquids.

[39] The mantle source of LCB, inferred from veins in Avacha xenoliths, is a highly refractory, opx- and Si-enriched harzburgite metasomatized by LILE-rich and (Nb, Ta)-poor slab-fluids.

[40] These inferences provide an alternative to current models, which argue that the trace element patterns of LCB magmas mimic those of slab-derived metasomatic components.

[41] LCB magmas may be produced at different stages of arc formation.

Acknowledgments

[42] C. Alboussière made thick sections. J. L. Devidal provided analytical assistance for EPMA and O. Bruguier for ICPMS measurements. Comments and advice from L. Danyushevsky and two anonymous reviewers considerably improved the clarity and quality of the manuscript. Editorial handling by Joel Baker is much appreciated.

References

Ayers, J. C., S. K. Dittmer, and G. D. Layne (1997), Partitioning of elements between peridotite and H_2O at 2.0–3.0 GPa and 900–1100°C and implication to models of subduction zone processes, *Earth Planet. Sci. Lett.*, *150*, 381–398, doi:10.1016/S0012-821X(97)00096-4.

Bédard, J. H. (1999), Petrogenesis of boninites from the Betts Cove ophiolite, Newfoundland, Canada: Identification of subducted source components, *J. Petrol.*, *40*, 1853–1889, doi:10.1093/petroj/40.12.1853.

Bodinier, J. L., and M. Godard (2003), Orogenic, ophiolitic, and abyssal peridotites, in *Treatise on Geochemistry*, vol. 2, *The Mantle and Core*, edited by R. W. Carlson, pp. 103–170, Elsevier, Amsterdam.

Bodinier, J. L., G. Vasseur, J. Vernieres, C. Dupuy, and J. Fabries (1990), Mechanisms of mantle metasomatism: Geochemical evidence from the Lherz orogenic peridotite, *J. Petrol.*, *31*, 597–628, doi:10.1093/petrology/31.3.597.

Brenan, J. M., H. F. Shaw, D. L. Phinney, and F. J. Ryerson (1994), Rutile-aqueous fluid partitioning of Nb, Ta, Hf, Zr, U and Th: Implications for high field strength element depletions in island-arc basalts, *Earth Planet. Sci. Lett.*, *128*, 327–339, doi:10.1016/0012-821X(94)90154-6.

Brenan, J. M., H. F. Shaw, F. J. Ryerson, and D. L. Phinney (1995), Mineral-aqueous fluid partitioning of trace elements at 900°C and 2.0 GPa: Constraints on the trace element chemistry of mantle and deep crustal fluids, *Geochim. Cosmochim. Acta*, *59*, 3331–3350, doi:10.1016/0016-7037(95)00215-L.

Bureau, H., and H. Keppler (1999), Complete miscibility between silicate melts and hydrous fluids in the upper mantle: Experimental evidence and geochemical implications, *Earth Planet. Sci. Lett.*, *165*, 187–196, doi:10.1016/S0012-821X(98)00266-0.

Cameron, W. E. (1989), Contrasting boninite–tholeïte associations from New Caledonia, in *Boninites and Related Rocks*, edited by A. J. Crawford, pp. 314–338, Unwin Hyman, London.

Cameron, W. E., E. G. Nisbet, and V. J. Dietrich (1979), Boninites, komatiites and ophiolitic basalts, *Nature*, *280*, 550–553, doi:10.1038/280550a0.

Crawford, A. J., and R. R. Keays (1987), Petrogenesis of Victorian cambrian tholeiites and implications for the origin of associated boninites, *J. Petrol.*, *28*, 1075–1109, doi:10.1093/petrology/28.6.1075.

Crawford, A. J., T. J. Falloon, and D. H. Green (1989), Classification, petrogenesis and tectonic setting of boninites, in *Boninites and Related Rocks*, edited by A. J. Crawford, pp. 2–49, Unwin Hyman, London.

Duggen, S., M. Portnyagin, J. Baker, D. Ulfbeck, K. Hoernle, D. Garbe-Schönberg, and N. Grassineau (2007), Drastic shift in lava geochemistry in the volcanic-front to rear-arc region of the Southern Kamchatkan subduction zone: Evidence for the transition from slab surface dehydration to sediment melting, *Geochim. Cosmochim. Acta*, *71*, 452–480, doi:10.1016/j.gca.2006.09.018.

Falloon, T. J., and L. V. Danyushevsky (2000), Melting of refractory mantle at 1.5, 2 and 2.5 GPa under anhydrous and H_2O-understaturated conditions: Implications for the petrogenesis of high-Ca boninites and the influence of subduction components on mantle melting, *J. Petrol.*, *41*, 257–283, doi:10.1093/petrology/41.2.257.

Gaetani, G. A., A. J. R. Kent, T. L. Grove, I. D. Hutcheon, and E. M. Stolper (2003), Mineral/melt partitioning of trace elements during hydrous peridotite partial melting, *Contrib. Mineral. Petrol.*, *145*, 391–405, doi:10.1007/s00410-003-0447-0.

Ghiorso, M. S., M. M. Hirschmann, P. W. Reiners, and V. C. Kress III (2002), The pMELTS: A revision of MELTS for improved calculation of phase relations and major element partitioning related to partial melting of the mantle to 3 GPa, *Geochem. Geophys. Geosyst.*, *3*(5), 1030, doi:10.1029/2001GC000217.

Gorbatov, A., V. Kostoglodov, G. Suárez, and E. Gordeev (1997), Seismicity and structure of the Kamchatka subduction zone, *J. Geophys. Res.*, *102*, 17,883–17,898, doi:10.1029/96JB03491.

Green, T. H., J. D. Blundy, J. Adam, and G. M. Yaxley (2000), SIMS determination of trace element partition coefficients between garnet, clinopyroxene and hydrous basaltic liquids at 2–7.7 GPa and 1080–1200°C, *Lithos*, *53*, 165–187, doi:10.1016/S0024-4937(00)00023-2.

Halama, R., I. Savov, R. Rudnick, and W. F. McDonough (2009), Insights into Li and Li isotope cycling and sub-arc metasomatism from veined mantle xenoliths, Kamchatka, *Contrib. Mineral. Petrol.*, *158*, 197–222, doi:10.1007/s00410-009-0378-5.

Hickey, R. L., and F. A. Frey (1982), Geochemical characteristics of boninite series volcanics-implications for their source, *Geochim. Cosmochim. Acta*, *46*, 2099–2115, doi:10.1016/0016-7037(82)90188-0.

Ionov, D. A. (2010), Petrology of mantle wedge lithosphere: New data on supra-subduction zone peridotite xenoliths from the andesitic Avacha volcano, Kamchatka, *J. Petrol.*, *51*, 327–361, doi:10.1093/petrology/egp090.

Ionov, D. A., L. Savoyant, and C. Dupuy (1992), Application of the ICP-MS technique to trace element analysis of peridotites and their minerals, *Geostand. Newsl.*, *16*, 311–315, doi:10.1111/j.1751-908X.1992.tb00494.x.

Ionov, D. A., G. Chazot, C. Chauvel, C. Merlet, and J.-L. Bodinier (2006), Trace element distribution in peridotite xenoliths from Tok, SE Siberian craton: A record of pervasive, multi-stage metasomatism in shallow refractory mantle, *Geochim. Cosmochim. Acta*, *70*, 1231–1260, doi:10.1016/j.gca.2005.11.010.

Ionov, D., A. Bénard, and P. Plechov (2011), Melt evolution in subarc mantle: Evidence from heating experiments on spinel-hosted melt inclusions in peridotite xenoliths from the andesitic Avacha volcano (Kamchatka, Russia), *Contrib. Mineral. Petrol.*, *162*, 1159–1174, doi:10.1007/s00410-011-0645-0.

Jenner, G. A. (1981), Geochemistry of high-Mg andesites from Cape Vogel, Papua New Guinea, *Chem. Geol.*, *33*, 307–332, doi:10.1016/0009-2541(81)90106-6.

Kamenetsky, V. S., A. V. Sobolev, S. M. Eggins, A. J. Crawford, and R. J. Arculus (2002), Olivine-enriched melt inclusions in chromites from low-Ca boninites, Cape Vogel, Papua New Guinea: Evidence for ultramafic primary magma, refractory mantle source and enriched components, *Chem. Geol.*, *183*, 287–303, doi:10.1016/S0009-2541(01)00380-1.

Kawamoto, T. (2006), Hydrous phases and water transport in the subducting slab, *Rev. Min. Petrol.*, *62*, 273–289, doi:10.2138/rmg.2006.62.12.

Keppler, H. (1996), Constraints from partitioning experiments on the composition of subduction-zone fluids, *Nature*, *380*, 237–240, doi:10.1038/380237a0.

Kessel, R., M. W. Schmidt, P. Ulmer, and T. Pettke (2005), Trace element signature of subduction-zone fluids, melts and supercritical liquids at 120–180 km depth, *Nature*, *437*, 724–727, doi:10.1038/nature03971.

Klemme, S., J. D. Blundy, and B. J. Wood (2002), Experimental constraints on major and trace element partitioning during partial melting of eclogite, *Geochim. Cosmochim. Acta*, *66*, 3109–3123, doi:10.1016/S0016-7037(02)00859-1.

König, S., C. Münker, S. Schuth, A. Luguet, J. Elis Hoffmann, and J. Kuduon (2010), Boninites as windows into trace element mobility in subduction zones, *Geochim. Cosmochim. Acta*, *74*, 684–704, doi:10.1016/j.gca.2009.10.011.

Le Bas, M. J. (2000), IUGS classification of the high-Mg and picritic volcanic rocks, *J. Petrol.*, *41*, 1467–1470, doi:10.1093/petrology/41.10.1467.

Manea, V. C., M. Manea, V. Kostoglodov, and G. Sewell (2005), Thermal models, magma transport and velocity anomaly estimation beneath southern Kamchatka, in *Plates, Plumes, and Paradigms*, edited by G. R. Foulger et al., *Spec. Pap. Geol. Soc. Am.*, *388*, 517–536, doi:10.1130/0-8137-2388-4.517.

McDade, P., J. D. Blundy, and B. J. Wood (2003), Trace element partitioning between mantle wedge peridotite and hydrous MgO-rich melt, *Am. Mineral.*, *88*, 1825–1831.

McDonough, W. F., and S.-S. Sun (1995), The composition of the Earth, *Chem. Geol.*, *120*, 223–253, doi:10.1016/0009-2541(94)00140-4.

Müntener, O., P. B. Kelemen, and T. L. Grove (2001), The role of H_2O during crystallization of primitive arc magmas under uppermost mantle conditions and genesis of igneous pyroxenites: An experimental study, *Contrib. Mineral. Petrol.*, *141*, 643–658, doi:10.1007/s004100100266.

Parkinson, I. J., and J. A. Pearce (1998), Peridotites from the Izu-Bonin-Mariana forearc (ODP Leg 125), Evidence for mantle melting and melt-mantle interaction in a supra-subduction zone setting, *J. Petrol.*, *39*, 1577–1618, doi:10.1093/petroj/39.9.1577.

Parman, S. W., and T. L. Grove (2004), Harzburgite melting with and without H_2O: Experimental data and predictive modeling, *J. Geophys. Res.*, *109*, B02201, doi:10.1029/2003JB002566.

Pearce, J. A., P. D. Kempton, G. M. Nowell, and S. R. Noble (1999), Hf-Nd element and isotope perspective on the nature and the provenance of mantle and subduction components in western pacific arc-basin systems, *J. Petrol.*, *40*, 1579–1611, doi:10.1093/petroj/40.11.1579.

Pilet, S., P. Ulmer, and S. Villiger (2010), Liquid line of descent of a basanitic liquid at 1.5 GPa: Constraints on the formation of metasomatic veins, *Contrib. Mineral. Petrol.*, *159*, 621–643, doi:10.1007/s00410-009-0445-y.

Reagan, M. K., et al. (2010), Fore-arc basalts and subduction initiation in the Izu-Bonin-Mariana system, *Geochem. Geophys. Geosyst.*, *11*, Q03X12, doi:10.1029/2009GC002871.

Smith, P. M., and P. D. Asimow (2005), Adiabat_1ph: A new public front-end to the MELTS, pMELTS, and pHMELTS models, *Geochem. Geophys. Geosyst.*, *6*, Q02004, doi:10.1029/2004GC000816.

Soustelle, V., A. Tommasi, S. Demouchy, and D. A. Ionov (2010), Deformation and fluid-rock interaction in the supra-subduction mantle: Microstructures and water contents in peridotite xenoliths from the Avacha volcano, Kamchatka, *J. Petrol.*, *51*, 363–394, doi:10.1093/petrology/egp085.

Taylor, R. N., R. W. Nesbitt, P. Vidal, R. S. Harmon, B. Auvray, and I. W. Croudace (1994), Mineralogy, chemistry and genesis of the boninite series volcanics, Chichijima, Bonin islands, Japan, *J. Petrol.*, *35*, 577–617, doi:10.1093/petrology/35.3.577.

Thompson, A. B., M. Aerts, and A. C. Hack (2007), Liquid immiscibility in silicate melts and related systems, *Rev. Mineral. Geochem.*, *65*, 99–127, doi:10.2138/rmg.2007.65.4.

Walker, D. A., and W. E. Cameron (1983), Boninite primary magmas: Evidence from the Cape Vogel peninsula, PNG, *Contrib. Mineral. Petrol.*, *83*, 150–158, doi:10.1007/BF00373088.